

Article

Impact of Hybrid-Electric Aircraft on Contrail Coverage

Feijia Yin ^{1,*} , Volker Grewe ^{1,2}  and Klaus Gierens ² 

¹ Faculty of Aerospace Engineering, Delft University of Technology, 2629HS Delft, The Netherlands; Volker.Grewe@dlr.de

² Deutsches Zentrum für Luft- und Raumfahrt, Institut für Physik der Atmosphäre, Oberpfaffenhofen, D-82234 Weßling, Germany; klaus.gierens@dlr.de

* Correspondence: f.yin@tudelft.nl

Received: 31 July 2020; Accepted: 9 October 2020; Published: 12 October 2020



Abstract: Aviation is responsible for approximately 5% of global warming and is expected to increase substantially in the future. Given the continuing expansion of air traffic, mitigation of aviation's climate impact becomes challenging but imperative. Among various mitigation options, hybrid-electric aircraft (HEA) have drawn intensive attention due to their considerable potential in reducing greenhouse gas emissions (e.g., CO₂). However, the non-CO₂ effects (especially contrails) of HEA on climate change are more challenging to assess. As the first step to understanding the climate impact of HEA, this research investigates the effects on the formation of persistent contrails when flying with HEA. The simulation is performed using an Earth System Model (EMAC) coupled with a submodel (CONTRAIL), where the contrail formation criterion, the Schmidt–Appleman criterion (SAC), is adapted to globally estimate changes in the potential contrail coverage (PCC). We compared the HEA to conventional (reference) aircraft with the same characteristics, except for the propulsion system. The analysis showed that the temperature threshold of contrail formation for HEA is lower; therefore, conventional reference aircraft can form contrails at lower flight altitudes, whereas the HEA does not. For a given flight altitude, with a small fraction of electric power in use (less than 30%), the potential contrail coverage remained nearly unchanged. As the electric power fraction increased, the reduction in contrail formation was mainly observed in the mid-latitudes (30° N and 40° S) or tropical regions and was very much localized with a maximum value of about 40% locally. The analysis of seasonal effects showed that in non-summer, the reduction in contrail formation using electric power was more pronounced at lower flight altitudes, whereas in summer the changes in PCC were nearly constant with respect to altitude.

Keywords: hybrid-electric aircraft; potential contrail coverage; Schmidt–Appleman criterion; degrees of hybridization

1. Introduction

Civil aviation satisfies modern society's needs for mobility and is an essential economic driver. Air transportation demand increases at around 4.4% per annum and is forecast to maintain that growth rate for the next few decades [1]. Although the global COVID-19 pandemic has put a great challenge on the aviation industry, we expect that aviation will eventually recover, as aviation has become a fundamental part of the modern world, providing long-range mobility. Aviation is responsible for approximately 5% of the anthropogenic causes of global warming [2], and it is expected to increase substantially in the future. Given the continuing expansion of air traffic, mitigation of aviation's climate impact becomes challenging but imperative.

An overview of the climate impact of aviation associated with various species/effects is presented in Figure 1 [3]. Both CO₂ and non-CO₂ effects from NO_x (ozone formation and methane depletion), water vapor, contrails, and direct aerosols are included. One can see that CO₂ emissions share less than half of the total aviation radiative forcing (RF), and the rest is from non-CO₂ effects. It is also noticeable that contrail cirrus is the largest contributor to the total aviation RF, with some uncertainties in the current level of understanding.

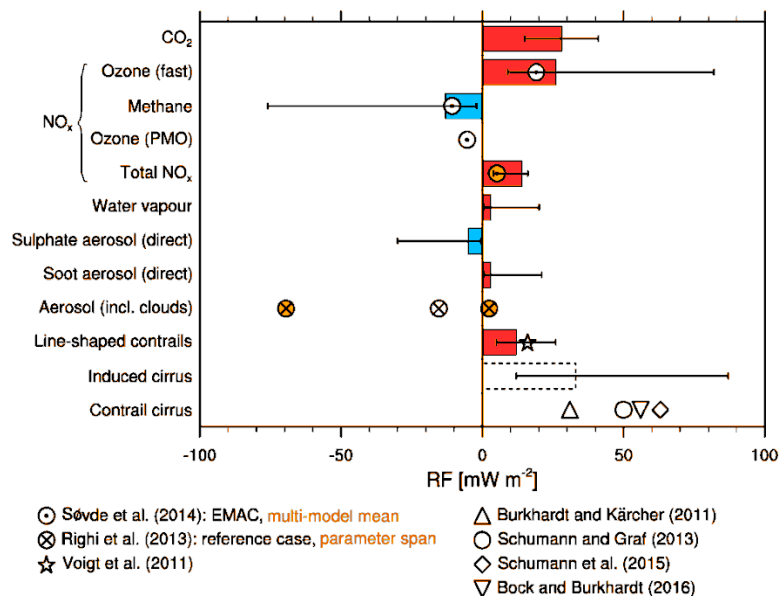


Figure 1. Aviation-induced radiative forcing from different components for the year 2005 [3–10].

Because of its long lifetime, aviation's climate impact from CO₂ is mainly determined by the amount of CO₂ emissions. The induced perturbation of the atmospheric CO₂ concentration is determined by several lifetimes that are associated with individual processes, such as land-uptake (biosphere; 1–100 years) and sediment formation (1000 to 10,000 years) [11]. Due to the long lifetimes, the concentration change can be estimated to first-order by accumulating CO₂ emissions over aviation history. On the contrary, the short-lived non-CO₂ effects depend not only on the emission quantity but also on the geographical location, altitude, time, and the local weather conditions. It is possible to mitigate aviation's climate impact via operational measures to avoid climate-sensitive regions associated with non-CO₂ effects, e.g., to contrail avoidance [12–17].

The formation of persistent contrails depends on environmental conditions and aircraft/engine technologies. The well-known Schmidt–Appleman criterion (SAC) [18,19] suggests that the possible measures to reduce aviation's contrail formation are reducing the H₂O emission index, increasing the fuel lower heating value, or decreasing the overall propulsion efficiency. Various options can affect these three measures, e.g., new aircraft design [20] and alternative fuels [21–24].

Electric aircraft is one of the possible options as well, since using a battery will eliminate exhaust emissions. Due to technology limitations, a purely electric aircraft would not be feasible. Instead, hybrid-electric aircraft is proposed for regional/narrow-body airliners [25,26]. For long-range flights, the electric propulsion system's additional weight makes it difficult to achieve substantial fuel saving. A hybrid-electric propulsion system consists of a gas turbine engine combined with an electric motor (EM) and a battery pack. There are several possible ways to connect these components in a power train. The most frequently proposed configurations are the series and parallel type, as demonstrated in Figure 2. In a series configuration, the gas turbine generates electricity via a generator. EM then uses the electricity to drive a fan/propeller. Batteries can assist in supplying power to the EM. In the parallel type, a gas turbine and EM drive the fan/propeller simultaneously, with different hybridization degrees. In addition, the operational flexibility of the parallel hybrid-electric system (HEPS) may allow

for full electrical power through the climate-sensitive regions, such as contrail-vulnerable parts of a flight, hence eliminating contrail formation.

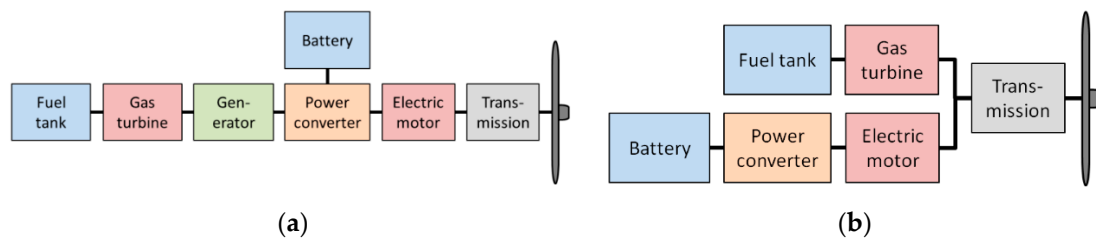


Figure 2. Schematic of a hybrid-electric propulsion system: (a) series configuration, (b) parallel configuration [27].

As the first step towards understanding the climate impact of hybrid-electric aircraft, this research investigates the effects on the formation of contrails when flying with hybrid-electric aircraft (HEA). A parallel hybrid configuration, as described in Figure 2b, is considered. In terms of the baseline aircraft, an earlier study suggested a possible mission range of 1000 km for a parallel hybrid-electric plane to allow reasonable benefits of fuel savings [26]. The A320 type aircraft is then our potential baseline. Figure 3 shows an example of a power management strategy for a parallel configuration. The degrees of hybridization between fuel and electricity can be varied to achieve different mission performance. For contrail avoidance, it would be better to have a 100% electric flight at the contrail-sensitive regions of the cruise flight only, which is analyzed in detail in the current paper.

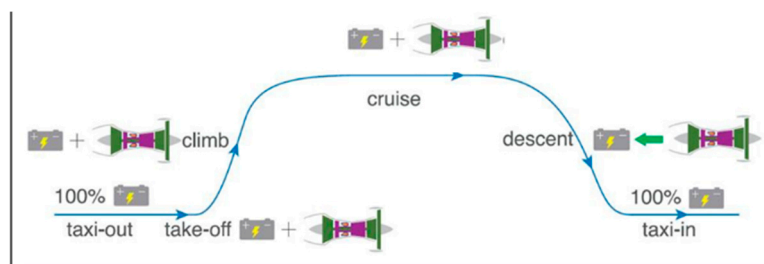


Figure 3. An example power management strategy adapted from [26]. During taxi-out/taxi-in phases, 100% electrical power is used, whereas during take-off, climb, and cruise conditions, battery and turbofan engine are used in parallel. The arrow on the mission profile indicates different flight stages.

The paper is organized as follows. In Section 2, the methods used to predict the potential contrail coverage (PCC), defined as the atmospheric ability to form contrails for a given aircraft and fuel type [28], are elaborated. The conditions of contrail formation for parallel hybrid-electric configuration are also discussed. Section 3 analyses the effects of the variation of cruise altitude, degrees of hybridization, and seasons on PCC changes. Finally, conclusions are drawn in Section 4.

2. Methodology

We have envisaged a research roadmap (as presented in Figure 4) to investigate the potential of flying a hybrid-electric plane for contrail avoidance. The complete research chain contains the relevant technical aspects of HEA for contrail formation (the green box), the PCC calculation procedure, the operational strategy of HEA to avoid contrails, and the actual mitigation potential when flying HEA. In this paper, we present the first steps of the roadmap (marked in blue). Subsequent research will cover the later steps (marked in orange). This section elaborates on the details of the methodology of the first steps (those in blue).

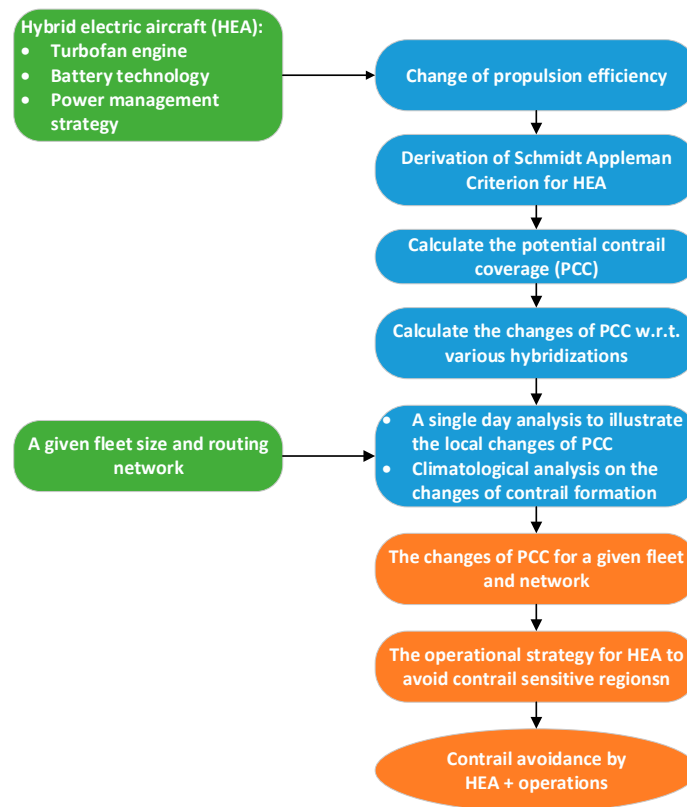


Figure 4. A schematic of a research methodology map to investigate the potentials of flying a hybrid-electric aircraft (HEA) for contrail avoidance.

An Earth System Model (EMAC) coupled with a CONTRAIL submodel was used to predict the hybrid-electric aircraft's PCC. The CONTRAIL submodel includes a revision of the contrail formation criterion for HEA. Please note that in this analysis, we focus on the contrails formed at the engine exhaust, whereas aerodynamic contrails are not considered. The formation of aerodynamic contrails mainly depends on the aerodynamic design of aircraft, especially the airfoil [29], which is assumed to be unchanged in this analysis and of minor importance concerning their climate impact [30].

2.1. The Base Model EMAC

The ECHAM/MESy Atmospheric Chemistry (EMAC) model is a numerical chemistry and climate simulation system that includes submodels describing tropospheric and middle atmosphere processes and their interaction with oceans, land, and human influences [31]. For the present study, we applied EMAC (ECHAM5 version 5.3.02, MESy version 2.52.0) in T42L31ECMWF-resolution, corresponding to a horizontal grid of about 310 km and a vertical resolution of roughly 1 km up to an altitude of approximately 30 km. The simulation time step is 12 min. Such a model resolution will provide us with reasonable weather data to calculate the potential contrail coverage.

EMAC has been extensively validated with other models, for instance, ACCMIP presented in [32], concerning atmospheric dynamics, cloud occurrence, chemistry, etc. An overview is given in [33]. In this paper, we use the submodel CONTRAIL V1.0. Section 2.2 discusses details on the CONTRAIL submodel.

2.2. The CONTRAIL Submodel

CONTRAIL is one of the submodels in EMAC, developed by Frömming et al. (supplement of [12]) to calculate the potential coverage of persistent contrails instantaneously, with the EMAC resolution specified in the previous section. The thermodynamic condition of contrail formation is given by the

Schmidt–Appleman criterion [18,19], the derivation of which is presented in Section 2.3 of this paper. In the CONTRAIL submodel, the PCC is calculated as the difference between the maximum possible coverage of both contrails and cirrus and the natural cirrus coverage alone. Supersaturation with respect to ice is used to determine if the contrails are persistent or not.

2.3. The HEA Extended Schmidt–Appleman Criterion

Contrails form when the mixture of engine exhaust and ambient air reaches water saturation at a sufficiently low temperature, and they persist when the ambient air is ice-supersaturated. The mixing process is assumed to be isobaric; therefore, the mixing trajectory is represented as a straight line on the T - e diagram (see Figure 1 of [34]; e is the partial pressure of water vapor in the mixture; T is the static temperature of the mixture). The slope of this straight line (G) determining the temperature threshold of contrail formation is given by the SAC and calculated using Equation (1).

$$G = \frac{p \cdot c_p \cdot EIH2O}{\varepsilon \cdot Q \cdot (1 - \eta_K)} \quad (1)$$

where p is the ambient pressure in Pa; ε is the ratio of the molar mass of water vapor and dry air (0.622 constant); c_p is the isobaric heat capacity of air (1004 J/kg/K); Q is the lower heating value of fuel in MJ/kg; $EIH2O$ is the water vapor emission index in kg/kg(fuel); and the notation (η_K) is the overall propulsion efficiency of the pure kerosene aircraft (reference), for which we assumed a value of 0.4 in the current study. This efficiency value was in line with the value computed using the aircraft/engine performance model presented in [27].

For HEA, the thrust power is provided by two energy sources, as defined by Equation (2).

$$FV = \eta_K \cdot \dot{m}_f \cdot Q + \eta_E \cdot P_E \quad (2)$$

where F is the thrust requirement in N, V is the flight speed in m/s, \dot{m}_f is the fuel flow rate of kerosene in kg/s, η_E is the overall efficiency of the aircraft when electric power is working alone, the notation (P_E) is the electric power in watts.

Accordingly, the original SAC was adapted using the assumption that kerosene plus electric power are combined to the necessary power FV results (details are discussed in Appendix A). The revised calculation procedure for slope G leads to Equation (3), which considers the effects of various degrees of hybridization.

$$G = \frac{c_p \cdot p_a}{\varepsilon} \frac{R \cdot EIH2O}{R(1 - \eta_K)Q + (1 - R)(1 - \eta_E)Q_E^0} \quad (3)$$

where $R\dot{m}_f / \dot{m}_{f_{max}}$. For the same thrust power, the maximum fuel flow rate ($\dot{m}_{f_{max}}$) corresponds to the fuel consumption of the reference aircraft, where only kerosene is used. Hence, at pure liquid-fuel operation, $R = 1$, and pure electric operation, $R = 0$. The notation (Q_E^0) is a quasi-electric energy content, defined in Equation (4):

$$Q_E^0 := Q \cdot (\eta_K / \eta_E) \quad (4)$$

Note that the SAC derivation in this paper only applies to the situation where batteries provide electric power. A battery has no water vapor emission. Suppose the electric power is provided by a fuel cell or another gas turbine via a generator. In that case, water vapor is emitted by these components. A different form of the Schmidt–Appleman criterion must be derived to consider the effects of water vapor emitted by, e.g., the fuel cell.

3. Results

3.1. The Threshold of Contrail Formation Calculated by SAC

On the basis of the SAC derivation in Section 2.3, we studied the threshold of contrail formation for HEA. Figure 5 shows how the contrail factor G varies with the share of electric propulsion. It is zero for pure electric propulsion ($R = 0$) and increases non-linearly with the fraction of liquid-fuel propulsion until it reaches its maximum at full liquid-fuel propulsion. The shape of the curve depends on the efficiency η_E of the electric powertrain. The higher is η_E , the flatter the relation close to $R = 1$.

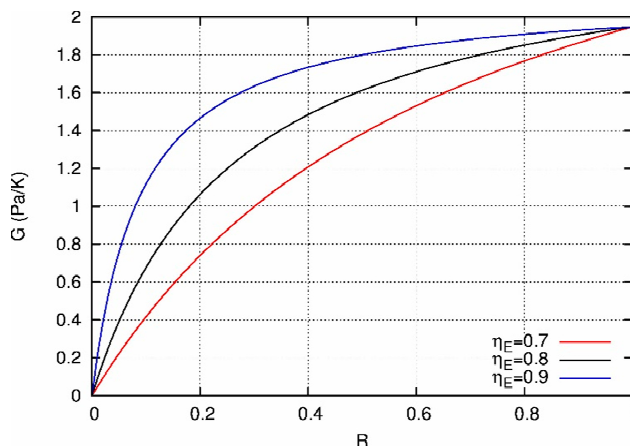


Figure 5. Dependence of the contrail factor G on the ratio R for parallel-hybrid-electric propulsion. $R = 1$ is full fuel propulsion, $R = 0$ is full electric propulsion. Parameters for the calculation have been $\eta_K = 0.4$, $Q = 43.2$ MJ/kg, $p_a = 250$ hPa, and $Q_E^0 = (\eta_K / \eta_E)Q$.

For the maximum temperature (T_{max}) ([35], Equation (5)), at which contrail formation is possible, we studied the effects of various η_E with respect to the fraction of electric power (see Figure 6). For a more efficient electric system with a high η_E , it needs a relatively high electric share (R is very small) to achieve a substantial lowering of T_{max} . In our example, the maximum temperature at which contrails can be formed when only liquid fuel is used ($R = 1$) is -40 °C. To reduce this by 5 K, to achieve a maximum temperature of -45 °C, it needs roughly $R = 0.3$, or 70% of the thrust power needs to be provided by the electric motor when its efficiency is 0.8. For the smaller efficiency, the reduction in T_{max} is larger. This may sound paradoxical, but it is the consequence of the simple physical fact that contrail formation is easier when the exhaust gas is colder, for what is higher combined overall propulsion efficiencies.

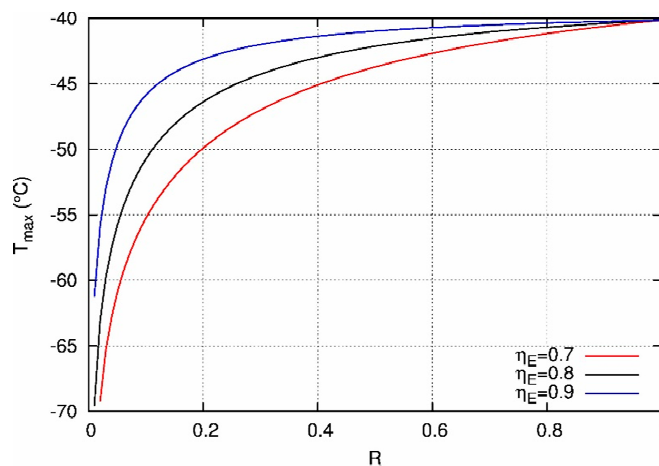


Figure 6. Dependence of the maximum temperature at which contrails are possible, T_{max} , on the ratio R for parallel-hybrid-electric propulsion. Parameters are as in Figure 4.

This paper considered the technology level of 2030 for electric motor, inverter, and battery, as summarized in [27,36]. Furthermore, a typical value of 0.9 for fan efficiency was used. Eventually, the value of η_E was about 0.8. This value was then used in the further analysis of PCC.

A further example of the parameters for SAC on different aircraft is presented in Table 1. The numbers were calculated for an altitude of 11 km. Figure 7 shows three critical mixing lines: one for conventional aircraft with an overall efficiency of 0.4, one for HEA with 40% electric power, and one for HEA with 80% electric power. These three mixing lines ran from the engine exhaust conditions and were tangential to the water saturation pressure line. At the same flight altitude, the temperature threshold and the slope G decreased with the increase of electric power in use. Therefore, the chance for HEA to form contrails reduced as the electric power fraction increased.

Table 1. Calculated parameters for the Schmidt–Appleman criterion on hybrid-electric aircraft.

Parameters	Descriptions	Hybrid-Electric Aircraft		Conventional Aircraft	Units
Electric power fraction		40%	80%	0	[-]
E_{H_2O}	Water emission index		1.25		kg/kg(fuel)
η	Overall efficiency	0.8		0.4	[-]
Q	The lower heating value of the fuel		43.2		MJ/kg
G	Slope at 11 km altitude	1.6	1.1	1.8	Pa/K

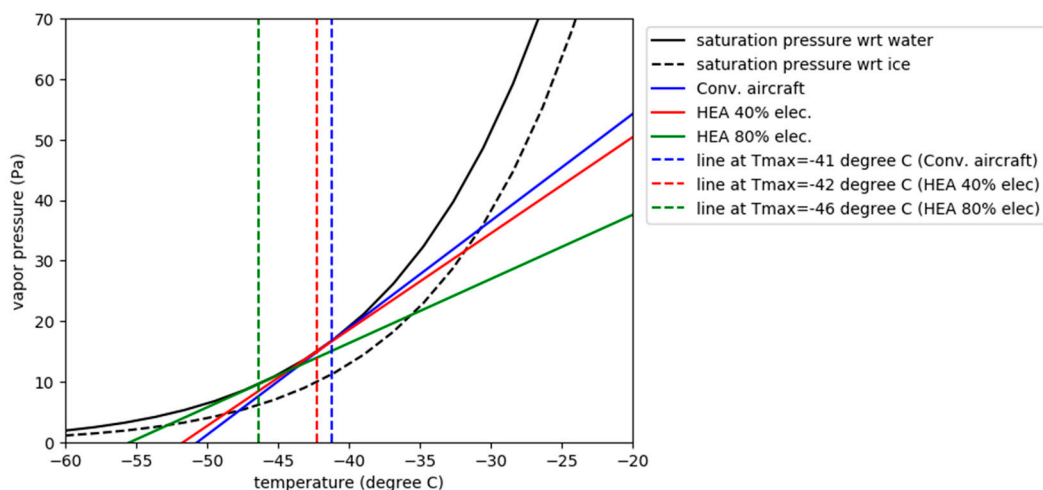


Figure 7. Mixing line for threshold conditions. Water vapor pressure vs. temperature phase diagram representing thermodynamics of contrail formation for a conventional aircraft with overall propulsion efficiency of 0.4 (blue line) and HEA with two different degrees of hybridization: 40% electric power (red line) and 80% electric power (green line). The two black curves are the saturation vapor pressure curves for water (solid) and with respect to ice (dashed). The vertical dashed lines represent the temperature threshold for the conventional aircraft (blue), HEA with 40% electric power (red), and HEA with 80% electric power (green).

3.2. Changes in Potential Contrail Coverage

We studied the variations of potential contrail coverage caused by different effects, for instance, altitude, degree of hybridization, and seasons. In this section, we present the results. The data are based on a one-year simulation with EMAC, including the updated CONTRAIL submodel (see above). For illustration purposes, we first present results for an arbitrary day in winter to give an impression of an actual weather situation and then present climatological values. All the results were obtained with 0.8 electric power efficiency and 0.4 kerosene system efficiency.

3.2.1. One-Day Case Study

Figure 8a shows the PCC of conventional aircraft at 300 hPa (FL300) on a specific day. In contrast, the changes in PCC caused by 50% electric hybridization of HEA (i.e., $R = 0.5$ in Equation (3)) at the same altitude is given in Figure 8b. For the pure kerosene case, the contrails were mainly formed at the mid-latitudes and polar regions, where the local temperature was sufficiently low to form contrails. With 50% thrust power supplied by the battery, the reduction in contrail formation was observed at about 30° N and 40° S, where the tropopause climbed to the higher altitudes. The local temperature in this region was close to the temperature threshold for the pure kerosene aircraft. A transition to HEA lowered the temperature threshold by a few degrees Celsius. It was also noticeable that the contrail formation's reduction was very much localized with a maximum value of around 0.4, which might have been related to the local temperature and humidity.

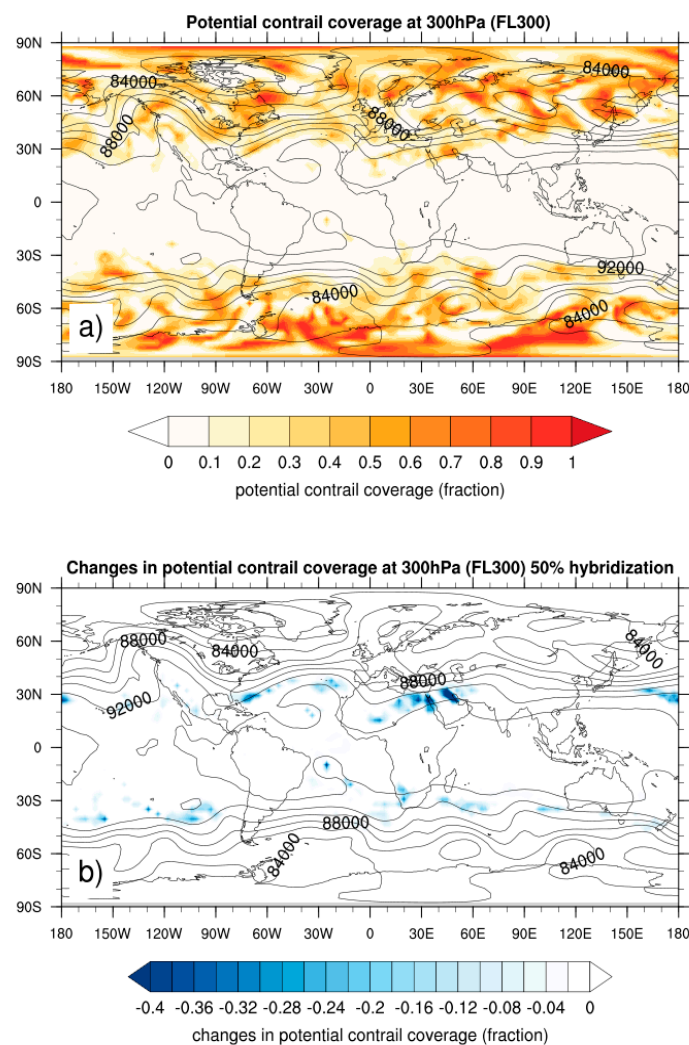


Figure 8. The potential contrail coverage (PCC) (contour) and geopotential (black contour; $\text{m}^2 \text{s}^{-2}$) at 300 hPa (FL300) on a specific day: (a) conventional aircraft; (b) absolute changes caused by HEA with 50% electric power.

When increasing the flight altitude from 300 hPa to 250 hPa (FL340), for the conventional reference aircraft, we found the areas of potential contrail coverage in the tropical regions as well (Figure 9a). For HEA, with 50% of electric hybridization, the reduction of contrail formation was more pronounced in the tropical regions, as seen in Figure 9b.

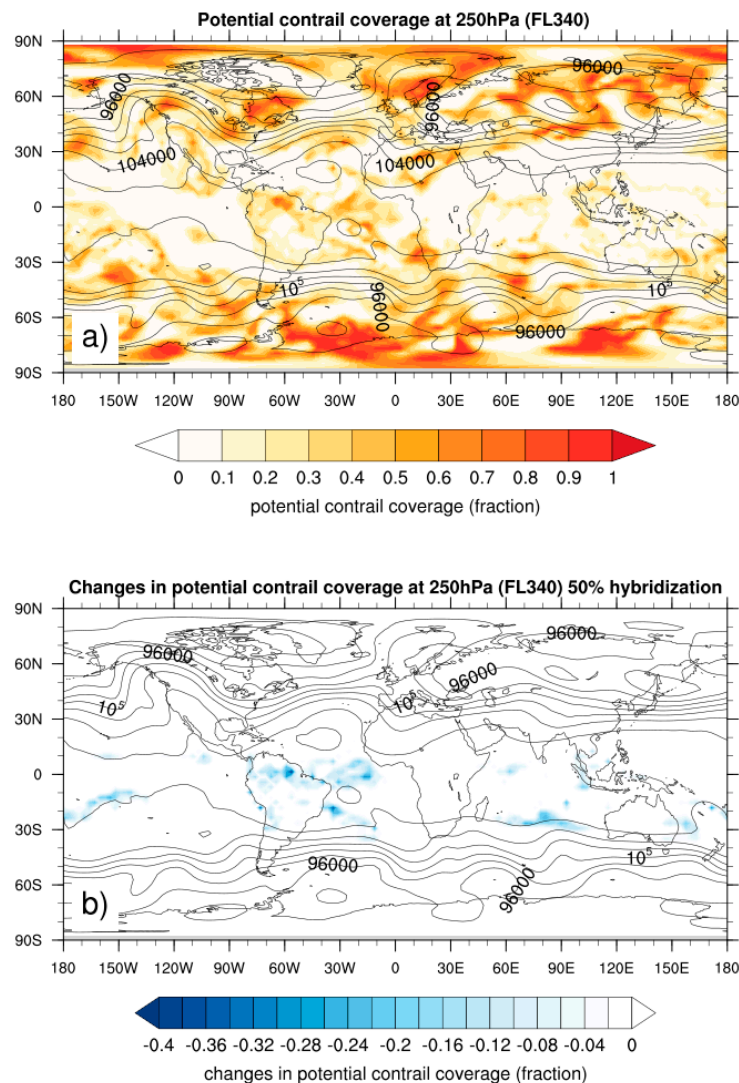


Figure 9. The PCC (contour) and geopotential (black contour; $m^2 s^{-2}$) at 250 hPa (FL340) on a specific day: (a) conventional aircraft; (b) absolute changes caused by HEA with 50% electric power.

When we increased the flight altitude further to 200 hPa (FL390), HEA with 50% of electric hybridization had no significant change in contrail formation. At this level, the ambient temperature was far below the threshold for contrail formation for conventional aircraft. HEA did not lead to a sufficient lowering of that temperature threshold with 50% electric power. However, increasing the hybridization to 90% allowed for a further reduction of the temperature threshold for contrail formation. Accordingly, a reduction in contrails was observed in several locations of the tropical region, as shown in Figure 10b.

3.2.2. Effect of Degree of Hybridization

In Figure 11, we present a statistical analysis of the local reduction of contrail coverage when different hybridization degrees were considered. The annual mean PCC was used. We observed that the contrail coverage remained nearly unchanged with a smaller fraction of electric power in use (less than 30%). As the hybridization rate increased from 10–90%, an exponential reduction trend was found, which was already indicated by the theoretical analysis in Figures 5 and 6.

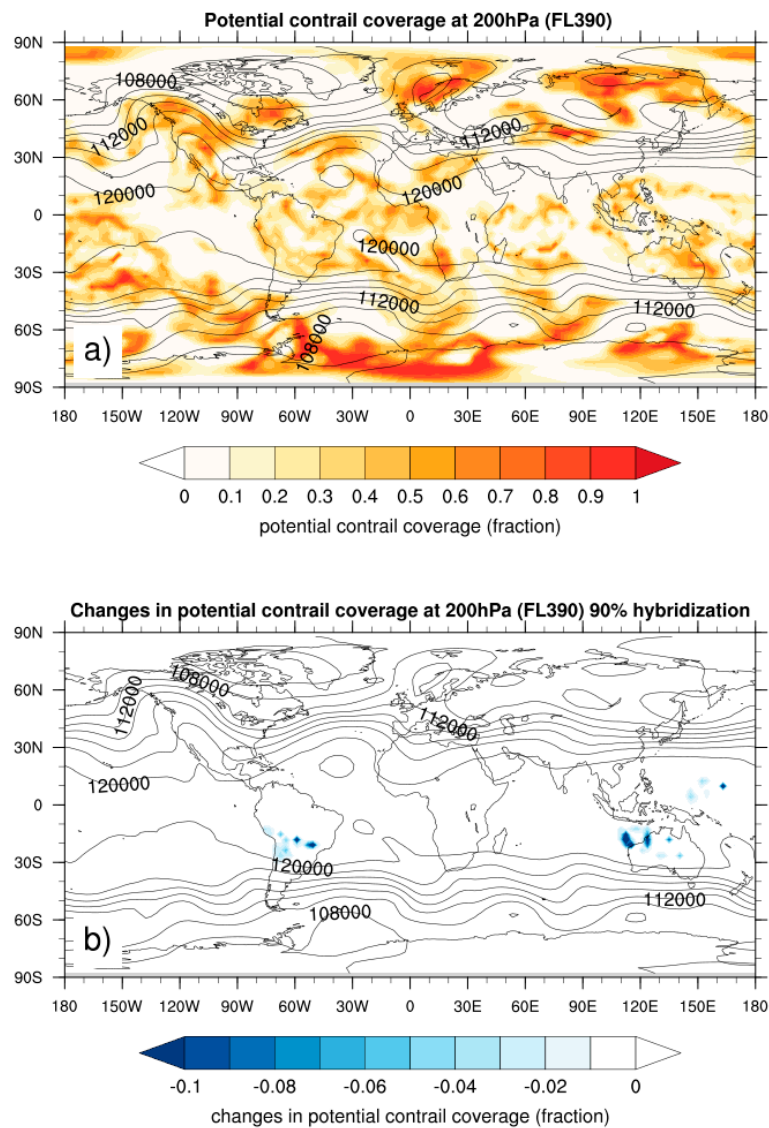


Figure 10. The PCC (contour) and geopotential (black contour; $m^2 s^{-2}$) at 200 hPa (FL390) on a specific day: (a) conventional aircraft; (b) absolute changes caused by HEA with 90% electric power.

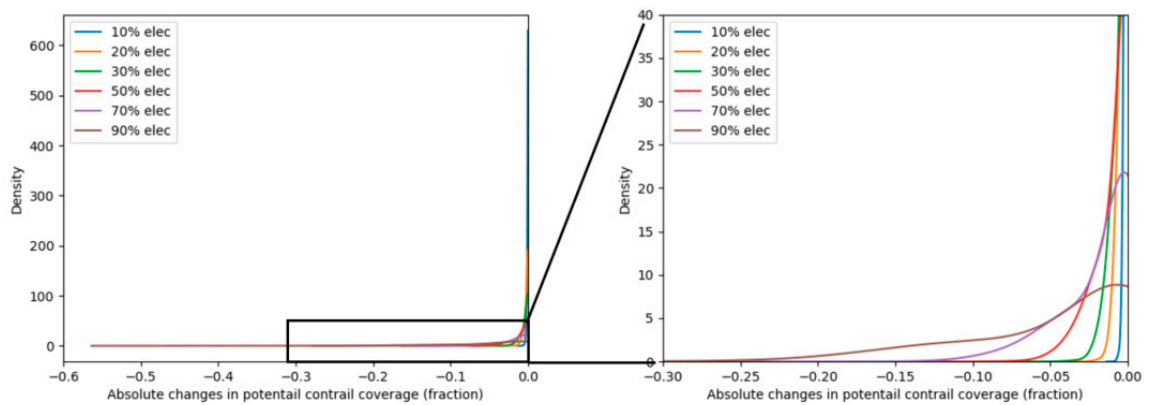


Figure 11. Distribution of the reduction in PCC with respect to different degrees of electric hybridization.

3.2.3. Climatology of Contrail Formation

The zonal annual mean values of PCC for the reference aircraft and various hybridization degrees are presented in Figure 12. Figure 12a shows the potential contrail coverage for the conventional aircraft, which was also used as a baseline to evaluate different degrees of hybridization effects. From Figure 12b–d, the degree of hybridization increased from 30% to 50% and up to 90%. Again, corresponding to the SAC theory, HEA did not form contrails at the higher temperature and could not form contrails in the lower region of the potential contrail coverage of conventional contrails. Therefore, the reduction of HEA in contrail formation occurred mostly at the lower flight altitudes. However, as the hybridization increased, the altitude range, where contrail formation was reduced, grew.

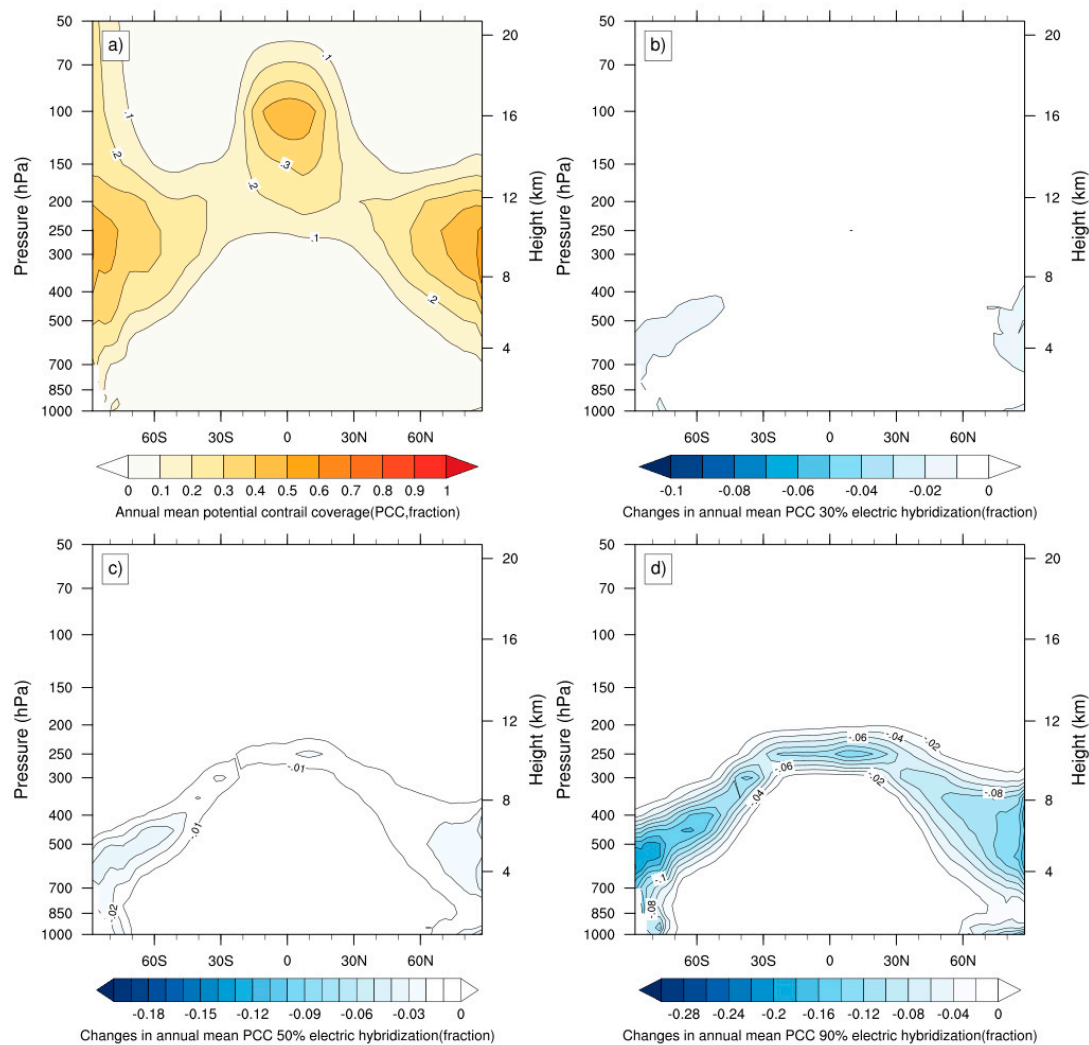


Figure 12. Annual zonal mean potential contrail coverage and changes due to electric hybridization: (a) conventional aircraft; (b) 30% electric hybridization; (c) 50% electric hybridization; (d) 90% electric hybridization.

3.2.4. Seasonal Effects

On the basis of the annual simulation results, we studied the seasonal effects. Figure 13 presents the variations in PCC for 90% of hybridization. The results were grouped into four seasons at four pressure altitudes. Generally, we expected the largest effect (i.e., the greatest reduction in PCC) on the lowest pressure level, since the temperatures on that level were closest to the SAC-temperature threshold.

Similarly, we expected the PCC reduction to become smaller towards higher pressure altitudes with their lower temperatures. This pattern was evident in the figure, except for summer. There were more substantial reductions on 150 hPa (FL450) and 200 hPa (FL390) levels in summer than in the other seasons. This behavior was partly due to higher temperatures, closer to the SAC-threshold, but lower relative humidity than those in different seasons may contribute to PCC reduction. The reduction was found to be more or less constant in summer at all flight levels (differences were insignificant), although the difference between the actual and the SAC-threshold temperature increased with flight level. It is likely that a decreasing frequency of high humidity (including ice-supersaturation) cases balanced the temperature effect such that the PCC reduction in summer depended little on the flight altitude.

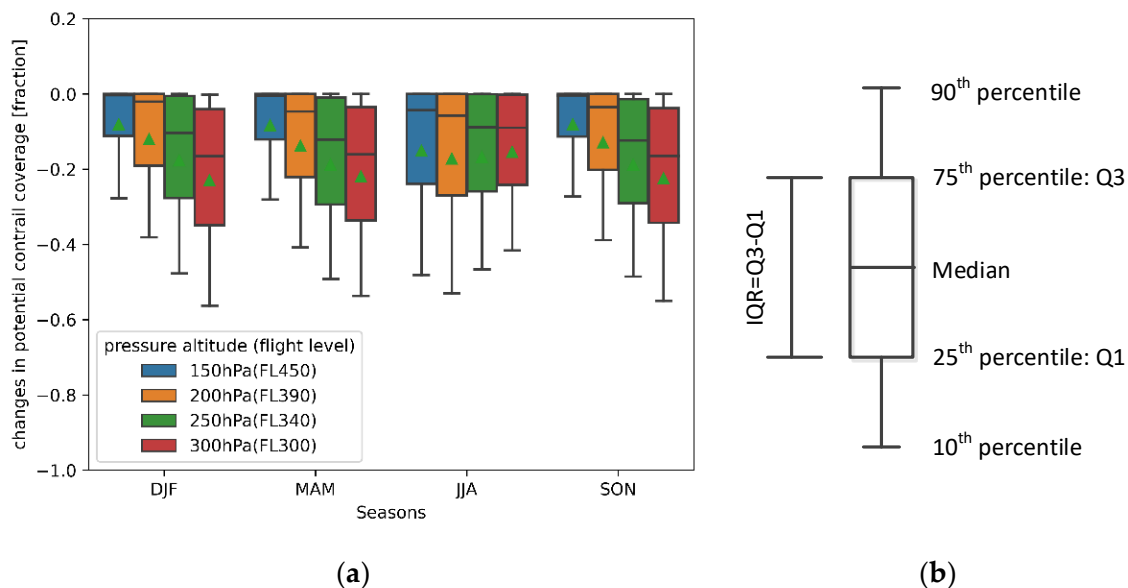


Figure 13. Seasonal effects on the changes of potential contrail coverage at various pressure altitudes for 90% electric hybridization (a) and the explanation of the boxplot (b). DJF: December, January, and February; MAM: March, April, and May; JJA: June, July, and August; SON: September, October, and November. For the boxplot: the 10th and 90th percentiles of the data are plotted. Triangle indicates the mean value. As the altitude increases, e.g., at 150 hPa (FL450), the values at 90th percentile and 75th percentile are equal to the minimum of the datasets as zero, therefore not visible in Figure (a).

4. Discussion

This study demonstrated the effects of hybrid-electric aircraft on potential contrail coverage. The actual contrail properties—the number of soot particles related to using a hybrid-electric propulsion system, the lifetime of contrails, etc.—were not considered. Earlier research shows that the number of soot particles produced by a turbofan engine is strongly dependent on the thrust setting [37]. A higher thrust setting would lead to an increase in the combustion temperature, hence, increasing the rate of soot formation, and vice versa. As different degrees of electric hybridization were considered, the gas turbine engine’s thrust setting and the number of soot particles varied accordingly. The change in soot particles will affect the contrails’ actual optical properties, thus the resulting contrail radiative forcing.

Furthermore, the Schmidt–Appleman criterion’s derivation in this paper is applicable for a hybrid-electric propulsion system, for which the electric power is generated by battery. If the choice goes for a fuel cell hybrid-electric propulsion system, one would require a different consideration. The SAC for the fuel cell type of hybrid system depends on how the fuel cell’s exhaust is handled. If a heat exchanger is used to collect the fuel cell’s exhaust heat, the water vapor at the fuel cell’s exhaust is then condensed into a liquid. In this case, contrails are only formed from the gas turbine exhaust. The SAC derivation in the current paper can still be valid. However, if no condensation process is

involved, the fuel cell then also produces water vapor in the exhaust, which must be considered to derivate an alternative SAC.

As observed from our analysis, the reduction in contrail coverage by hybrid-electric aircraft is mostly localized. The consequences are twofold. In a case where the flight route does not cross a region of reduction (that is, the temperature is significantly lower than the contrail formation threshold even for a high portion of electric power), flying with a hybrid-electric aircraft does not affect the contrail formation. Still, the contrail properties (lifetime, optical thickness, and eventually individual radiative forcing) may change with the degree of hybridization. In another case where the contrail reduction is possible along the flight route (that is, the temperature is close to the contrail formation threshold), using a large fraction of electric power at that specific location would effectively reduce contrail formation. For the second case, a specific power management strategy can be developed to design the hybrid-electric system. Eventually, we expect the actual effect to be a convolution of the existing air traffic patterns with the PCC-reduction patterns. In further analysis, we will investigate the effectiveness of contrail avoidance by hybrid-electric aircraft, considering the routing effects.

In addition, in our analysis, we used a typical value of 0.4 as the overall propulsion efficiency, and we left it constant regardless of the amount of electrical power used. As more electrical energy is used, the gas turbine engine's thrust setting is reduced; correspondingly, the propulsion efficiency would decrease slightly. If we consider such efficiency deterioration, the temperature threshold of contrail formation for the hybrid-electric system is reduced further (see, e.g., Equation (1) and Figure 6 of this paper). The lower temperature threshold implies that contrail formation is more likely to decrease, but it requires a thorough analysis in future research.

5. Conclusions

This paper presents the changes in potential contrail coverage when flying with hybrid-electric aircraft. On the basis of the analysis, we have drawn the following conclusions:

- The atmospheric areas of contrail formation of hybrid-electric aircraft are smaller than those of conventional aircraft and require lower atmospheric temperatures.
- The reduction in contrail formation by hybrid-electric aircraft is more pronounced in a tropical region where the temperatures are higher.
- With a small degree of hybridization (below 30% in the current study), the contrail coverage remains nearly unchanged. A maximum reduction of about 40% in contrail coverage was observed locally, with 90% electric power in use.
- In non-summer, the reduction in potential contrail coverage by hybrid-electric aircraft was more noticeable at lower flight altitudes. In contrast, the changes in potential contrail coverage were nearly constant (about 20%) for all flight altitudes studied in summer.

Author Contributions: Conceptualization of this study, V.G. and F.Y.; derivation of the Schmidt–Appleman criterion for hybrid-electric aircraft, V.G. and K.G.; formal analysis and writing the original draft, F.Y.; writing—review, V.G. and K.G.; funding acquisition, V.G. and F.Y. All authors have read and agreed to the published version of the manuscript.

Funding: Initial work received funding from the SESAR Joint Undertaking under grant agreement no. 699395 under the European Union's Horizon 2020 research and innovation program within the Exploratory Research project ATM4E. The individual author of this work receives funding from the Dutch Research Council (NWO) under the talent scheme VENI and in-kind contribution from DLR-Oberpfaffenhofen. The project number is 17367.

Conflicts of Interest: The authors declare no conflict of interest.

Nomenclature

Abbreviations

DJF	December, January, and February	
EIH ₂ O	Water vapor emission index	kg/kg(fuel)
EM	Electric motor	
HEA	Hybrid-electric aircraft	
JJA	June, July, and August	
MAM	March, April, and May	
PCC	Potential contrail coverage	
PDF	Probability density function	
RF	Radiative forcing	
SAC	Schmidt–Appleman criterion	
SON	September, October, and November	

Symbols

c_p	Isobaric heat capacity of the air	J/kg/K
F	Thrust	N
G	The slope of the mixing line	pa/K
\dot{m}_f	Fuel mass flow rate	kg/s
p	Ambient pressure	pa
P_E	Electric power	W
Q	The lower heating value of fuel	MJ/kg
R	Degrees of hybridization	[–]
T_{max}	The maximum temperature at which contrail formation is possible	°C
V	Velocity	m/s
ε	The ratio of the molar mass of water vapor and dry air	[–]
η_E	The overall efficiency of the electric powertrain	[–]
η_K	The overall efficiency of the pure kerosene aircraft	[–]

Appendix A. Derivation of Schmidt–Appleman Criterion for Hybrid-Electric Aircraft

The thermodynamic theory of contrail formation was developed for traditional jet engines many years ago [18,19]. A modern derivation is provided by [35] using the conservation principles of mass, momentum and energy. The traditional engine type has only one source of energy, namely, the fuel with its specific energy content Q . For each kilogram of fuel burnt, a mass of EIH_2O kilogram water vapor is produced and emitted. For a fuel flow rate of \dot{m}_{fuel} , the rate of water vapor emission is $\dot{m}_{fuel}EIH_2O$.

The condition for contrail formation is the Schmidt–Appleman criterion (SAC). The most important factor in the theory is the so-called contrail factor $G = de_p/dT_p$, that is, the change of partial pressure of water vapor in the exhaust plume, e_p , with plume temperature, T_p . This change occurs when the plume is expanding and mixing with ambient air. This mixing is isobaric at ambient pressure, p_a , and the mixing trajectory of the exhaust gases in a thermodynamic, $e - T$, diagram is thus a straight line with slope G . The endpoint of that trajectory at infinite mixing is represented by the ambient conditions: water vapor partial pressure, e_a , and temperature, T_a . Thus we find

$$G = \frac{e_p - e_a}{T_p - T_a} \quad (A1)$$

It is practical to use mass mixing ratios $q_x = \varepsilon e_x/p_a$, where $\varepsilon = 0.622$ is the ratio of molar masses of H_2O and air. The partial pressure of water vapor at the engine exit is

$$e_p = \frac{p_a}{\varepsilon} \cdot \frac{\dot{m}_a q_a + \dot{m}_f \cdot EIH_2O}{\dot{m}_a + \dot{m}_f} \quad (A2)$$

where the notation (\dot{m}_a) is the mass flow rate of air through the engine. In this derivation, we do not consider the separation of the core flow and bypass flow, as the two air streams mix anyway at the engine exit within a few milliseconds. Such a consideration will avoid an unnecessary complication of the equations. The equation states

that the vapor partial pressure at the engine exit is composed of that carried by the air needed to burn the fuel plus the contribution from the fuel itself. Since an electric motor does not emit water vapor, there is hence no contribution. Thus, the numerator in the formula for G is

$$e_p - e_a = \frac{p_a}{\varepsilon} \cdot \frac{\dot{m}_f \cdot (EIH_2O - q_a)}{\dot{m}_a + \dot{m}_f} \approx \frac{p_a}{\varepsilon} \cdot \frac{\dot{m}_f \cdot EIH_2O}{\dot{m}_a + \dot{m}_f} \quad (A3)$$

where the approximation is possible since $EIH_2O \gg q_a$.

The aircraft needs a thrust F to overcome drag and friction. When it flies with a velocity V , the engines must produce a power

$$FV = \eta_K \cdot \dot{m}_f \cdot Q + \eta_E \cdot P_E \quad (A4)$$

That is, two sources of energy, from the liquid fuel and the electric motor, add their powers with their respective thermodynamic efficiencies, η_x . The notation (P_E) is the (variable) power of the electric engine. P_E varies in response to variable fuel flow, such that the above sum equals FV . Thus, P_E is a function of \dot{m}_f .

$$P_E = P_E^0 - a \cdot \dot{m}_f \text{ with } P_E^0 = FV/\eta_E \text{ and } a = Q \cdot (\eta_K/\eta_E) \quad (A5)$$

Here, P_E^0 is the electric power when it is driving the aircraft alone. The higher the fuel flow, the lower P_E is. The maximum fuel flow to achieve a thrust power of FV is $\dot{m}_{f_{max}} = FV/\eta_K Q$. It turns out to be useful also to define a quasi-electric energy content, namely,

$$Q_E^0 := P_E^0/\dot{m}_{f_{max}} = a = Q(\eta_K/\eta_E) \quad (A6)$$

As the efficiencies are never 1.0, the remaining part of the produced power is wasted for heating and expelling the exhaust gases (from the burnt fuel and the air flowing through the engine). These are thermal and kinetic energies. For the present derivation, we neglected the kinetic energy since it is much smaller than the thermal energy. Thus, we have

$$(1 - \eta_K)\dot{m}_f Q + (1 - \eta_E)P_E = c_p [\dot{m}_a (T_p - T_a) + \dot{m}_f T_p] \quad (A7)$$

That is, the engine air is heated from its ambient temperature to the plume temperature, and the gas added by burning the liquid fuel is heated to T_p as well. (A few other energy sources and sinks are neglected here: the enthalpy of the liquid fuel, the heating of the engine parts, for instance). The symbol (c_p) is the heat capacity (at constant pressure) of air. After a few steps, we find

$$T_p - T_a = \frac{(1 - \eta_K)\dot{m}_f Q + (1 - \eta_E)P_E - c_p \dot{m}_f T_a}{c_p (\dot{m}_a + \dot{m}_f)} \approx \frac{(1 - \eta_K)\dot{m}_f Q + (1 - \eta_E)P_E}{c_p (\dot{m}_a + \dot{m}_f)} \quad (A8)$$

This approximation is possible since the enthalpy of the ambient air is much smaller than the energy content of the fuel or the energy produced by the electric motor. Dividing Equation (A3) by Equation (A8) gives an expression for the contrail factor

$$G = \frac{c_p p_a}{\varepsilon} \cdot \frac{\dot{m}_f \cdot EIH_2O}{(1 - \eta_K)\dot{m}_f Q + (1 - \eta_E)P_E(\dot{m}_f)} \quad (A9)$$

where the dependence of P_E on the fuel flow is made explicit for clarity.

Now it appears convenient to normalize the fuel flow rate by its maximum,

$$R := \dot{m}_f / \dot{m}_{f_{max}} \quad (A10)$$

At pure liquid-fuel operation, $R = 1$, and at pure electric operation, $R = 0$. Having this and the other definitions from above, we arrive after a few steps at a favorable expression for G :

$$G = \frac{c_p p_a}{\varepsilon} R \frac{EIH_2O}{R(1 - \eta_K)Q + (1 - R)(1 - \eta_E)Q_E^0} \quad (A11)$$

Equation (A11) is the desired expression. It has the correct limiting properties. For $R = 1$ we retain the form of the traditional SAC, but for pure electric propulsion, $R = 0$, hence, $G = 0$, which implies that contrail formation is impossible.

From here, it is relatively straightforward to formulate a generalization to more than two energy sources. Let

$$FV = \eta_K \dot{m}_f Q + \sum_i \eta_i P_i \quad (\text{A12})$$

where apart from the liquid fuel, we have a number of energy sources (index i) that do not produce water in the exhaust. Then we introduce in analogy to the derivation above:

$$P_i^0 := FV / \eta_i, \quad Q_i^0 := P_i^0 / \dot{m}_{f,max} = (\eta_K / \eta_i) Q \quad (\text{A13})$$

Furthermore, we define weights $w_i P_i / P_i^0$. It can then be shown that

$$\sum_i w_i = 1 - R \quad (\text{A14})$$

With these prerequisites, we finally arrive at a straightforward generalization of Equation (A11):

$$G = \frac{c_p P_a}{\varepsilon} R \frac{EI_{H2O}}{R(1 - \eta_K)Q + \sum_i w_i (1 - \eta_i) Q_i^0} \quad (\text{A15})$$

References

1. Airbus. *Global Market Forecast: Global Networks, Global Citizens 2018–2037*; Airbus: Toulouse, France, 2018.
2. Lee, D.S.; Fahey, D.W.; Forster, P.M.; Newton, P.J.; Wit, R.C.N.; Lim, L.L.; Owen, B.; Sausen, R. Aviation and global climate change in the 21st century. *Atmos. Environ.* **2009**, *43*, 3520–3537. [[CrossRef](#)] [[PubMed](#)]
3. Grewe, V.; Dahlmann, K.; Flink, J.; Frömming, C.; Ghosh, R.; Gierens, K.; Heller, R.; Hendricks, J.; Jöckel, P.; Kaufmann, S.; et al. Mitigating the Climate Impact from Aviation: Achievements and Results of the DLR WeCare Project. *Aerospace* **2017**, *4*, 34. [[CrossRef](#)]
4. Burkhardt, U.; Kärcher, B. Global radiative forcing from contrail cirrus. *Nat. Clim. Chang.* **2011**, *1*, 54. [[CrossRef](#)]
5. Søvde, O.A.; Matthes, S.; Skowron, A.; Iachetti, D.; Lim, L.; Owen, B.; Hodnebrog, Ø.; Di Genova, G.; Pitari, G.; Lee, D.S.; et al. Aircraft emission mitigation by changing route altitude: A multi-model estimate of aircraft NOx emission impact on O3 photochemistry. *Atmos. Environ.* **2014**, *95*, 468–479. [[CrossRef](#)]
6. Voigt, C.; Schumann, U.; Jessberger, P.; Jurkat, T.; Petzold, A.; Gayet, J.F.; Krämer, M.; Thornberry, T.; Fahey, D.W. Extinction and optical depth of contrails. *Geophys. Res. Lett.* **2011**, *38*. [[CrossRef](#)]
7. Schumann, U.; Graf, K. Aviation-induced cirrus and radiation changes at diurnal timescales. *J. Geophys. Res. Atmos.* **2013**, *118*, 2404–2421. [[CrossRef](#)]
8. Bock, L.; Burkhardt, U. Reassessing properties and radiative forcing of contrail cirrus using a climate model. *J. Geophys. Res. Atmos.* **2016**, *121*, 9717–9736. [[CrossRef](#)]
9. Righi, M.; Hendricks, J.; Sausen, R. The global impact of the transport sectors on atmospheric aerosol: Simulations for year 2000 emissions. *Atmos. Chem. Phys.* **2013**, *13*, 9939–9970. [[CrossRef](#)]
10. Schumann, U.; Penner, J.E.; Chen, Y.; Zhou, C.; Graf, K. Dehydration effects from contrails in a coupled contrail–climate model. *Atmos. Chem. Phys.* **2015**, *15*, 11179–11199. [[CrossRef](#)]
11. Ciais, P.; Sabine, C.; Bala, G.; Bopp, L.; Brovkin, V.; Canadell, J.; Chhabra, A.; DeFries, R.; Galloway, J.; Heimann, M.; et al. *Carbon and Other Biogeochemical Cycles*; Cambridge University Press: Cambridge, UK; New York, NY, USA, 2013.
12. Grewe, V.; Frömming, C.; Matthes, S.; Brinkop, S.; Ponater, M.; Dietmüller, S.; Jöckel, P.; Garny, H.; Tsati, E.; Dahlmann, K. Aircraft routing with minimal climate impact: The REACT4C climate cost function modelling approach (V1. 0). *Geosci. Model Dev.* **2014**, *7*, 175–201. [[CrossRef](#)]
13. Matthes, S.; Grewe, V.; Dahlmann, K.; Frömming, C.; Irvine, E.; Lim, L.; Linke, F.; Lührs, B.; Owen, B.; Shine, K.; et al. A Concept for Multi-Criteria Environmental Assessment of Aircraft Trajectories. *Aerospace* **2017**, *4*, 42. [[CrossRef](#)]
14. Campbell, S.E.; Bragg, M.B.; Neogi, N.A. Fuel-Optimal Trajectory Generation for Persistent Contrail Mitigation. *J. Guid. Control. Dyn.* **2013**, *36*, 1741–1750. [[CrossRef](#)]
15. Zou, B.; Buxi, G.S.; Hansen, M.J.N.; Economics, S. Optimal 4-D Aircraft Trajectories in a Contrail-sensitive Environment. *Netw. Spat. Econ.* **2016**, *16*, 415–446. [[CrossRef](#)]

16. Hartjes, S.; Hendriks, T.; Visser, D. Contrail Mitigation Through 3D Aircraft Trajectory Optimization. In Proceedings of the 16th AIAA Aviation Technology, Integration, and Operations Conference, Washington, DC, USA, 13–17 June 2016. [[CrossRef](#)]
17. Yin, F.; Grewe, V.; Frömming, C.; Yamashita, H. Impact on flight trajectory characteristics when avoiding the formation of persistent contrails for transatlantic flights. *Transp. Res. Part D Transp. Environ.* **2018**, *65*, 466–484. [[CrossRef](#)]
18. Appleman, H. The formation of exhaust condensation trails by jet aircraft. *Bull. Am. Meteorol. Soc.* **1953**, *34*, 14–20. [[CrossRef](#)]
19. Schmidt, E. Die Entstehung von Eisnebel aus den Auspuffgasen von Flugmotoren. *Schriften der Deutschen Akademie der Luftfahrtforschung* **1941**, *5*, 1–15.
20. Faggiano, F.; Vos, R.; Baan, M.; Dijk, R.V. Aerodynamic Design of a Flying V Aircraft. In Proceedings of the 17th AIAA Aviation Technology, Integration, and Operations Conference, Denver, CO, USA, 5–9 June 2017. [[CrossRef](#)]
21. Brand, J.; Sampath, S.; Shum, F.; Bayt, R.L.; Cohen, J. Potential use of hydrogen in air propulsion. In Proceedings of the AIAA/ICAS International Air and Space Symposium and Exposition: The Next 100 Y, Dayton, OH, USA, 14–17 July 2003.
22. Pohl, H.W.; Malychev, V.V. Hydrogen in future civil aviation. *Int. J. Hydrogen Energy* **1997**, *22*, 1061–1069. [[CrossRef](#)]
23. Janic, M. Is liquid hydrogen a solution for mitigating air pollution by airports? *Int. J. Hydrogen Energy* **2010**, *35*, 2190–2202. [[CrossRef](#)]
24. Yin, F.; Gangoli Rao, A.; Bhat, A.; Chen, M. Performance assessment of a multi-fuel hybrid engine for future aircraft. *Aerosp. Sci. Technol.* **2018**, *77*, 217–227. [[CrossRef](#)]
25. Gladin, J.C.; Perullo, C.; Tai, J.C.; Mavris, D.N. A Parametric Study of Hybrid Electric Gas Turbine Propulsion as a Function of Aircraft Size Class and Technology Level. In Proceedings of the 55th AIAA Aerospace Sciences Meeting, Grapevine, TX, USA, 9–13 January 2017. [[CrossRef](#)]
26. Ang, A.W.X.; Gangoli Rao, A.; Kanakis, T.; Lammen, W. Performance analysis of an electrically assisted propulsion system for a short-range civil aircraft. *Proc. Inst. Mech. Eng. Part G J. Aerosp. Eng.* **2019**, *233*, 1490–1502. [[CrossRef](#)]
27. Holsteijn, M.R.V.; Rao, A.G.; Yin, F. Operating characteristics of an electrically assisted turbofan engine. In Proceedings of the AMSE Turbo Expo: Turbomachinery Technical Conference & Exposition, London, UK, 21–25 September 2020.
28. Sausen, R.; Gierens, K.; Ponater, M.; Schumann, U. A diagnostic study of the global distribution of contrails Part I: Present day climate. *Theor. Appl. Climatol.* **1998**, *61*, 127–141. [[CrossRef](#)]
29. Gierens, K.; Kärcher, B.; Mannstein, H.; Mayer, B. Aerodynamic Contrails: Phenomenology and Flow Physics. *J. Atmos. Sci.* **2009**, *66*, 217–226. [[CrossRef](#)]
30. Gierens, K.; Dilger, F. A climatology of formation conditions for aerodynamic contrails. *Atmos. Chem. Phys.* **2013**, *13*, 10847–10857. [[CrossRef](#)]
31. Jöckel, P.; Kerkweg, A.; Pozzer, A.; Sander, R.; Tost, H.; Riede, H.; Baumgaertner, A.; Gromov, S.; Kern, B. Development cycle 2 of the Modular Earth Submodel System (MESSy2). *Geosci. Model Dev.* **2010**, *3*, 717–752. [[CrossRef](#)]
32. Lamarque, J.-F.; Dentener, F.; McConnell, J.; Ro, C.-U.; Shaw, M.; Vet, R.; Bergmann, D.; Cameron-Smith, P.; Dalsoren, S.; Doherty, R.; et al. Multi-model mean nitrogen and sulfur deposition from the Atmospheric Chemistry and Climate Model Intercomparison Project (ACCMIP): Evaluation of historical and projected future changes. *Atmos. Chem. Phys.* **2013**, *13*, 7997–8018. [[CrossRef](#)]
33. Jöckel, P.; Tost, H.; Pozzer, A.; Kunze, M.; Kirner, O.; Brenninkmeijer, C.A.M.; Brinkop, S.; Cai, D.S.; Dyroff, C.; Eckstein, J.; et al. Earth System Chemistry integrated Modelling (ESCiMo) with the Modular Earth Submodel System (MESSy) version 2.51. *Geosci. Model Dev.* **2016**, *9*. [[CrossRef](#)]
34. Gierens, K.; Lim, L.; Eleftheratos, K. A Review of Various Strategies for Contrail Avoidance. *Open Atmos. Sci. J.* **2008**, *2*, 1–7. [[CrossRef](#)]
35. Schumann, U.M. Influence of Propulsion Efficiency on Contrail Formation. *Aerosp. Sci. Technol.* **2000**, *4*, 391–401. [[CrossRef](#)]
36. Varyukhin, A.N.; Suntsov, P.S.; Gordin, M.V.; Zakharchenko, V.S.; Rakhmankulov, D.Y. Efficiency Analysis of Hybrid Electric Propulsion System for Commuter Airlines. In Proceedings of the 2019 International Conference on Electrotechnical Complexes and Systems (ICOECS), Ufa, Russia, 21–25 October 2019; pp. 1–3. [[CrossRef](#)]

37. Boies, A.M.; Stettler, M.E.J.; Swanson, J.J.; Johnson, T.J.; Olfert, J.S.; Johnson, M.; Eggersdorfer, M.L.; Rindlisbacher, T.; Wang, J.; Thomson, K.; et al. Particle Emission Characteristics of a Gas Turbine with a Double Annular Combustor. *Aerosol Sci. Technol.* **2015**, *49*, 842–855. [[CrossRef](#)]



© 2020 by the authors. Licensee MDPI, Basel, Switzerland. This article is an open access article distributed under the terms and conditions of the Creative Commons Attribution (CC BY) license (<http://creativecommons.org/licenses/by/4.0/>).